

Research Paper

Magnetic Heating Stimulated Cargo Release with Dose Control using Multifunctional MR and Thermosensitive Liposome

Sayoni Ray¹, Chi-An Cheng^{2*}, Wei Chen^{1*}, Zhao Li^{1*}, Jeffrey I. Zink¹✉, Yung-Ya Lin¹✉

1. Department of Chemistry and Biochemistry, University of California, Los Angeles, CA 90095, USA
2. Department of Bioengineering, University of California, Los Angeles, CA 90095, USA

*Co-second authors; these authors contributed equally to this work.

✉ Corresponding authors: zink@chem.ucla.edu (Jeffrey I. Zink), yylin@chem.ucla.edu (Yung-Ya Lin)

© Ivyspring International Publisher. This is an open access article distributed under the terms of the Creative Commons Attribution (CC BY-NC) license (<https://creativecommons.org/licenses/by-nc/4.0/>). See <http://ivyspring.com/terms> for full terms and conditions.

Received: 2018.12.06; Accepted: 2019.04.04; Published: 2019.04.19

Abstract

Rationale: Magnetic resonance imaging (MRI) is one of the most widely used diagnostic tools in the clinic. In this setting, real-time monitoring of therapy and tumor site would give the clinicians a handle to observe therapeutic response and to quantify drug amount to optimize the treatment. In this work, we developed a liposome-based cargo (cancer drugs) delivery strategy that could simultaneously monitor the real-time alternating magnetic field-induced cargo release from the change in MRI relaxation parameter R_1 and the location and condition of liposome from the change in R_2 . The tumor site can then be monitored during the cargo release because liposomes would passively target the tumor site through the enhanced permeability and retention (EPR) effect. Physical insights from the experimental results and corresponding Monte Carlo spin dynamics simulations were also discussed.

Methods: Superparamagnetic iron oxide (SPIO) nanoparticles, diethylenetriaminepentaacetic acid gadolinium(III) (Gd(III)-DTPA), and a model cancer drug (fluorescein) were co-loaded in PEGylated thermosensitive liposomes. The liposomes were characterized by transmission electron cryo-microscopy (cryoTEM), dynamic light scattering (DLS), and inductively coupled plasma optical emission spectrometry (ICP-OES). Alternating magnetic field (AMF) was used to create controlled mild hyperthermia (39–42°C) and facilitate controlled cargo (fluorescein) release from the thermosensitive liposomes. MRI relaxation parameters, R_1 and R_2 , were measured at room temperature. The temporal variation in R_1 was used to obtain the temporal profile of cargo release. Due to their similar sizes, both the gadolinium and cargo (model cancer drug fluorescein) would come out of the liposomes together as a result of heating. The temporal variation in R_2 was used to monitor SPIO nanoparticles to enhance the tumor contrast. Monte Carlo spin dynamics simulations were performed by solving the Bloch equations and modeling SPIO nanoparticles as magnetized impenetrable spheres.

Results: TEM images and DLS measurements showed the diameter of the liposome nanoparticle ~ 200 nm. AMF heating showed effective release of the model drug. It was found that R_1 increased linearly by about 70% and then saturated as the cargo release process was completed, while R_2 remained approximately constant with an initial 7%-drop and then recovered. The linear increase in R_1 is consistent with the expected linear cargo release with time upon AMF heating. Monte Carlo spin dynamics simulations suggest that the initial temporal fluctuation of R_2 is due to the plausible changes of SPIO aggregation and the slow non-recoverable degradation of liposomal membrane that increases water permeability with time by the heating process. The simulations show an order of magnitude increase in R_2 at higher water permeability.

Conclusion: We have performed MR parameter study of the release of a cargo (model cancer drug, fluorescein) by magnetic heating from thermosensitive multifunctional liposomes loaded with dual contrast agents. The size of the liposome nanoparticles loaded with model cancer drug (fluorescein), gadolinium chelate, and SPIO nanoparticles was appropriate for a variety of cancer therapies. A careful and detailed analysis with theoretical explanation and simulation was carried out to investigate the correlation between MRI relaxation parameters, R_1 and R_2 , and different cargo release fractions. We have quantified the cargo release using R_1 , which shows a linear relation between each other. This result provides a strong basis for the dosage control of drug delivered. On the other hand, the fairly stable R_2 with almost constant value suggests that it could be used to monitor the position and condition of the liposomal site, as SPIO nanoparticles mostly remained in the aqueous core of the liposome. Because our synthesized SPIO-encapsulated liposomes could be targeted to tumor site passively by the EPR effect, or actively through magnetofection, this study provides a solid ground for developing MR cancer theranostics in combination of this nanostructure and AMF heating strategy. Furthermore, our simulation results predict a sharp increase in R_2 during the AMF heating, which opens up the exciting possibility of high-resolution, high-contrast real-time imaging of the liposomal site during the drug release process, provided AMF heating could be incorporated into an MRI setup. Our use of the clinically approved materials, along with confirmation by theoretical simulations, make this technique a promising candidate for translational MR cancer theranostics.

Key words: magnetic resonance theranostics, magnetic hyperthermia, alternating magnetic field (AMF), AMF-controlled drug release, thermosensitive multifunctional liposome

Introduction

Cancer is the second highest leading cause of death worldwide, after cardiovascular diseases. Recently developed cancer theranostic approaches provide a promising direction to detect and treat cancer simultaneously [1–6]. This kind of molecular therapeutics, coupled with biomedical imaging, enhances the scope and efficacy of the treatment. For example, one of the major challenges to treat cancer by chemotherapy is to deliver the required high dose at tumor sites while minimizing the toxic effects on the benign tissues. Nanoparticle-mediated targeted and controlled drug delivery along with real-time imaging could achieve the desired result by reducing harmful effects on the benign tissues.

Nanovehicles of optimum size, functionality to target tumor cells, and capability to carry both the drug and contrast agent and deliver drugs at the tumor site under external signaling are required for such a theranostic procedure [7–9]. Various kinds of nanovehicles have been developed recently for the purpose of targeted delivery and controlled drug release [7–15]. Among them, promising candidates are liposomes [16–22] that have shown appealing features for drug delivery, biocompatibility, and clinical efficiency. Pharmacokinetic properties of the drug are significantly altered after encapsulation in the liposome and the toxicity of the drug is substantially reduced [23]. Furthermore, the drug is restricted from early activation during the circulation process. Different formulations of liposomes are now in clinical trial or already clinically approved [23–31]. They have been shown to be effective to decrease the off-target toxicity on other tissues. For example, liposomal anthracycline delivery reduces cardiotoxicity [23]. However, no significant increase in the therapeutic efficacy has so far been found in the clinical trials [23].

To alleviate this problem, liposome extravasation and bioavailability could be increased with the use of mild hyperthermia (39–42°C) [23, 32–35]. Moreover, by increasing the concentration of drug at the tumor site through the leaky vascular permeability, chemotherapy at a slightly higher temperature has shown improved efficacy of the drugs. It has been found that a series of drugs show improved efficiency by heat activation. The synergistic effect of hyperthermia and chemotherapy are far more effective than the monotherapies [36–40]. The enhanced efficiency of the drugs has been attributed to the higher level of tumor perfusion, resulting in increased sensitivity to the tumor area [23]. Recent studies also showed that under mild hyperthermia, heat shock proteins released during cell necrosis acted as a trigger for antitumor immunity, thus regressing the tumor and reducing metastasis [41]. Hence, a combination of mild hyperthermia and significantly increased amount of drug delivery at the tumor site while

reducing any interaction of the drugs with the healthy tissues along with simultaneous monitoring of the drug release and tumor site would be a vastly improved form of chemotherapy that could considerably improve the efficiency of the treatment.

Hyperthermia can be created by different methods such as a water bath [34], high intensity focused ultrasound (HIFU) [42–44], and alternating magnetic field (AMF) induced heat [45–48]. However, water baths could not provide spatially accurate treatment and HIFU is restricted in its ability for deep thermal therapy to a large area or penetrating bone and air. Here, the use of AMF to create mild hyperthermia has the advantages of achieving high accuracy in a specific area along with higher penetration capability, which is an alternative approach for disrupting the blood brain barrier [49]. Most importantly, as an ongoing project in our group, the AMF facility could be integrated into the existing MRI instrumentation and radio-frequency amplifiers for MR theranostics to simultaneously treat the cancer by using AMF and monitor the cancer treating process.

To complete such a drug delivery scheme, it is essential to have an efficient real-time monitoring system to observe and control the drug release at the target site [50–53]. MRI is a powerful noninvasive imaging modality in this regard, which has no harmful radiation and has general clinical acceptance. Previous studies have shown the single-modal MRI-guided drug delivery systems [34, 43, 54, 55]. However, it is important to monitor simultaneously both the drug release and tumor site for an effective therapy. Dual-modal imaging is recommended over single-modal, as the latter could provide more handle to the clinicians to optimize the personalized treatment for better point-of-care. Combination of other imaging modalities might increase the scope of such treatments [56–58]. However, it is often restricted by high-energy ionizing radiation or limited penetration through the body. Hence, dual-modality within the scope of MRI could eliminate such restrictions for a successful treatment.

In clinical settings, clinicians mainly rely on either positive contrast T₁-weighted imaging or negative contrast T₂-weighted imaging. However, a combination of both could provide insights on both the pathological phenomena and soft tissue anatomy to improve MR cancer imaging for stage detection, early diagnosis, and vascular imaging [59]. Therefore, many studies have turned to the design of encapsulating dual-modal MRI contrast agents in different formulations of liposomes and other nanocarriers [44, 60–68]. For example, Bos and coworkers [44] have shown the encapsulation of superparamagnetic iron oxide (SPIO) nanoparticles and Gd-chelate (ProHance) in liposomes for dual

modal MRI. They have demonstrated *in vivo* HIFU treatment and discussed corresponding relaxation parameter changes. Other studies include different formulation of dual-modal MR contrast agents, such as synthesis of gadolinium and iron oxide-conjugated nanoparticles [61], surface functionalization of SPIO-encapsulated liposome with gadolinium chelates [64, 67], size-controlled iron oxide nanoparticles [63] etc. Novel nanoparticle formulations with iron and manganese were developed for dual modal imaging and future theranostic purposes [68].

In this work, we have encapsulated SPIO nanoparticles, diethylenetriaminepentaacetic acid gadolinium(III) dihydrogen salt hydrate (Gd(III)-DTPA, commercially known as Magnevist) molecules, and a commonly used small molecule model cancer drug (a fluorophore tracer, fluorescein [48, 69–71]) into the thermosensitive liposome nanoparticles. We have demonstrated real-time AMF-controlled fluorescein release under mild hyperthermia and done a careful characterization of dual MRI parameters – longitudinal relaxation rate (R_1) and transverse relaxation rate (R_2) with different amounts of cargo (fluorescein) release, as shown schematically in **Figure 1**. Gd(III)-DTPA molecules are released simultaneously with the cargo (fluorescein), changing R_1 and making it sensitive to the percentage of cargo release. R_2 parameter monitors SPIO nanoparticles. We have done detailed analysis and explained the correlation between the relaxation parameters and cargo release with mathematical modelling and Monte Carlo spin dynamics simulations. Synthesized liposomes could be efficiently targeted to specific tumor sites through magnetic force [72, 73] or active targeting [16, 74]. Hence, this work serves as a proof of concept for future MR theranostic approach, which could simultaneously fulfill all three important needs: 1) on demand cargo release using AMF-controlled mild hyperthermia; 2) monitoring

the position and condition of liposomal accumulation site (such as tumor) throughout the measurement by monitoring R_2 ; 3) dosage control of the cargo release process by monitoring R_1 parameter. Although we demonstrated our method using a model drug, existing *in vivo* and *in vitro* cancer drug release data and the associated diffusion models [75, 76] provide a strong basis for the validity of our results for real cancer drug release in animal body.

Here, we have used clinically approved formulations, so it has the potential to get readily adapted with magnetofection or any existing targeting approach. Theoretical simulations were carried out to understand the dynamical process during the AMF heating and a qualitative confirmation has been reached. The expected sharp rise in R_2 with slightly increased water permeability of liposome, as seen from the simulations, indicates the possibility of high-resolution, high-contrast MR imaging of the liposomal site in *in situ* measurements.

Materials and Methods

Preparation of hydrating solution

Dextran-coated iron oxide nanoparticles of diameter 5-10 nm with 10 mg/ml concentration were bought from Ocean Nanotech, USA. 0.5 ml of iron oxide solution was added to 1.5 ml of phosphate buffer saline (PBS, 100 mM) (Sigma Aldrich) containing Gd (III)-DTPA (Sigma Aldrich) and fluorescein (Sigma Aldrich) to obtain a 2 ml hydrating solution with a final concentration of 200 mM Gd (III)-DTPA and 100 mM fluorescein at pH 7.4.

Synthesis of liposome nanoparticles

A total of 40 micromole of 1,2-dipalmitoyl-sn-glycero-3-phosphocholine (DPPC) (Avanti Polar Lipids, Inc.), 1,2-distearoyl-sn-glycero-3-phosphocholine (DSPC) (Corden Pharma), Cholesterol (Sigma Aldrich), and 1,2-distearoyl-sn-glycero-3-phosphoethanolamine-N-[amino(polyethylene-glycol)-2000] (DSPE-PEG(2000)) (Corden Pharma) in a molar ratio of 67:15:13:5 were dissolved in chloroform/methanol (2:1) (Sigma Aldrich) mixture to yield an uniform solution of density between 10-20 mg/ml. The homogeneous solution was evaporated under high vacuum at 40°C and kept for 5 hours in a rotatory evaporator for complete evaporation of the organic solvent. The produced thin film was hydrated with hydrating solution containing iron oxide nanoparticles, Gd(III)-DTPA, and fluorescein at pH 7.4 for 1 hour in a rotatory evaporator at a constant speed at 65°C. The resulting solution was passed through 400 nm (31

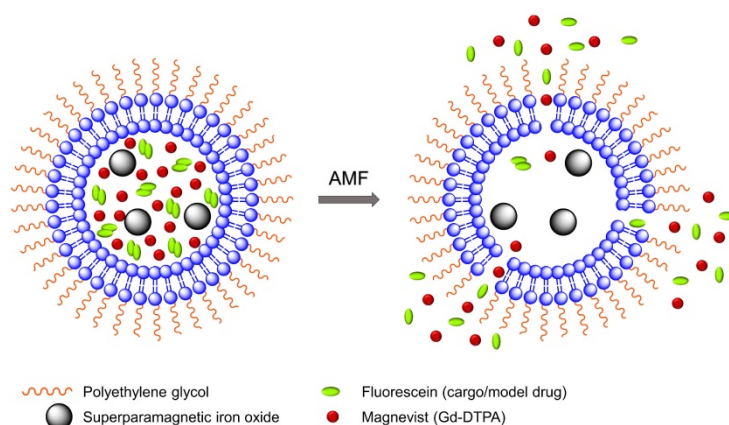


Figure 1. A schematic diagram of model drug/cargo (fluorescein) and contrast agents (magnetic nanoparticles and Gd(III)-DTPA) released from thermosensitive PEGylated liposomes under mild hyperthermia with alternating magnetic field (AMF). It illustrates the liposomes membrane permeability change and release of Gd(III)-DTPA and fluorescein upon AMF-induced heating.

times) and 100 nm (51 times) filters, respectively, during extrusion using a mini extruder (Avanti Polar Lipid, Inc.). Non-entrapped iron oxide nanoparticles, Gd(III)-DTPA, and fluorescein were removed by repeated washing using Sephadex G-25M PD-10 (Sigma Aldrich). The liposome solution was further purified by repeated filtration through 0.1 μm Amicon low-binding Durapore PVDF membrane (Millipore Corporation, Bedford, MA) at a centrifuge speed of 2000 rpm.

Material characterization

The size and zeta potential analysis were performed by dynamic light scattering (DLS) using a Zetasizer Nano (Malvern Instruments Ltd., Worcestershire, U.K.). The sizes of the liposome nanoparticles were measured before and after heating in 100 mM PBS buffer. Zeta potential of the liposome solution was recorded in the deionized water. The morphology, distribution, and size of liposome nanoparticles were determined by transmission electron cryomicroscopy (CryoTEM). Grids were made by taking 2.5 μl of the liposome sample on a glow-discharged Quantifoil holey-carbon grid (SPI Quantifoil R1.2/1.3) [77]. The grids were subsequently blotted dry and about 100 nm thick residual film of suspended solution across the holes in the grids was obtained by using a manual plunger. This solution was then rapidly plunged frozen around -196°C into a 2:1 mixture of liquid propane: liquid ethane to produce a vitrified glassy solution within the holes. This quick freezing produced an amorphous ice-containing sample in the holey carbon film. The grid was then loaded with Gatan cryo specimen holder into FEI Titan Krios (Electron Imaging Center for NanoMachines, California NanoSystems Institute) microscope for imaging. The images were acquired by operating the machine at 200 kV with a TIETZ F415MP 16 megapixel CCD camera.

The concentration of iron (Fe) or Gadolinium (Gd) were quantitatively determined by inductively coupled plasma optical emission spectrometry (ICP-OES) using a Shimadzu ICPE-9000 instrument. Different concentrations of liposome samples and supernatant solution were digested overnight with a 10 mL of aqua regia at 95°C . Afterward, the solution was diluted with a 2% of HNO_3 solution for quantitative measurement. The calibration curves for Fe or Gd were obtained from 0 ppm to 10 ppm and the results were fitted to obtain Fe and Gd amounts.

AMF-controlled cargo (model drug fluorescein) release

The set up was the same as described in the previous studies [47, 48]. Superparamagnetic heating was executed using a Magnetic Hyperthermia System manufactured by MSI Automation Inc. A five-turn copper coil (both the height and diameter = 50 mm) was used for the experiment. The magnetic field oscillation frequency, amplitude, and induction power were 375 kHz, 20 kA/m, and 5 kW, respectively. The fluorescence spectra were acquired using an Acton Spectra Pro 2300i CCD cooled below -120°C with liquid nitrogen. CUBE 445-40C laser (Coherent Inc., Santa Clara, CA, USA) was used for excitation at a wavelength of 448 nm and a power of 4 mW. Scattered and stray light beams were blocked with a long pass filter.

Synthesized liposome solution was diluted 10 times with 100 mM PBS buffer. 1 ml of the solution was exposed to AMF for 105 minutes. The fluorescence yield of fluorescein was measured after cooling the sample to room temperature at the end of each 15 minutes of AMF induced heating cycle. AMF heating would continuously increase the bulk temperature of the sample. The bulk temperature of the sample was measured using a thermometer at the end of each AMF induced 15-minute heating cycle. Thus, the measured temperature is the maximum temperature achieved at the end of the cycle. Each time, 50 μL of the sample was added to 3.5 ml of PBS buffer (100 mM) in a standard 1 cm fluorescence cuvette. The intensity around the fluorescein emission maximum was integrated over the wavelength range from 510 nm – 520 nm for three scans. The process was repeated three times and averaged over three such integrated emission spectra. The errors were computed from the standard deviation of three measurements. The fluorescence spectra of PBS were recorded in an identical way and used as the background for all the analyses.

In order to determine the percentage of cargo release as a result of AMF heating, the sample was completely lysed with a solution of 60 μL of 10% triton X-100 and fluorescence spectra were acquired. The fluorescence spectra were acquired for 10% Triton added PBS buffer and a background spectrum for triton was obtained without adding the sample to the triton solution. The percentage of cargo release in each case was calculated according to the equation [45]:

$$\text{Cargo release (\%)} = \frac{\left(\text{Fluorescence of AMF treated sample} - \text{Fluorescence before AMF treatment} \right)}{\left(\text{Fluorescence after lysing with Triton} - \text{Fluorescence of Triton Background} \right)} \times 100\%$$

Tracking MRI parameters

The samples with different cargo release were collected and the relaxation rates were measured using a 600 MHz (AV600, Bruker) Nuclear Magnetic Resonance (NMR) spectrometer and micro-imaging setup. The relaxation rates of the sample after complete lysing by Triton X-100 were also measured. R_1 was measured using the saturation recovery pulse sequence and R_2 was measured by the CPMG (Carr-Purcell-Meiboom-Gill) pulse sequence. The relaxation delay time was varied from 5-15 s, depending on the samples and the number of scans was = 1. The saturation time was 300 ms and time of recovery was ranging from 5 ms to 10 s for saturation recovery pulse sequence. For CPMG pulse sequence, half of the interval between successive 180° pulses (τ_{CP}) was = 500 μ s and time of echo (TE) was ranging from 2 to 100 ms. Each measurement was repeated three times and the average value was taken. The errors were calculated from the standard deviation of the three measurements. All measurements were performed at room temperature.

The background relaxation rates were measured from the supernatant obtained after precipitating all the liposomes by centrifugation (20,000 g). The supernatant had been checked with TEM and DLS to ensure it was free from liposomes. The background correction was done on the relaxation rate and the corrected relaxation rates were determined for each sample. Percentage change in the relaxation rates were calculated as follows:

$$\text{Change in Relaxation rate (\%)} = \frac{\{(\text{Sample relaxation rate} - \text{Background relaxation rate}) - (\text{Initial relaxation rate before heating} - \text{Background relaxation rate})\}}{\text{Initial relaxation rate before heating} - \text{Background relaxation rate}} \times 100\%$$

Longitudinal relaxivity (r_1) and transverse relaxivity (r_2) were deduced from the measurement of relaxation rates at different dilutions before and after completing magnetic heating and corrected by the background relaxation rate as follows:

$$\text{Corrected relaxation rate} = \text{Sample relaxation rate} - \text{Background relaxation rate}$$

Corrected Fe and Gd concentrations were obtained from ICP-OES measurements according to the equation:

$$\text{Corrected concentration} = \text{Sample concentration} - \text{Background concentration}$$

The corrected relaxation rates were plotted with the corrected concentration and a linear fit was obtained. The relaxivity parameter was obtained from the slope of the fitted straight line.

Monte Carlo spin dynamics simulations

Monte Carlo spin dynamics simulations using a diffusion model were performed to calculate R_2 parameter for different inter-nanoparticle separation of SPIO aggregations and water permeability of liposome membrane. SPIO nanoparticles were modeled as magnetized impenetrable spheres of radius = 5 nm. Based on cryoTEM images, we estimated that there were 7 SPIO nanoparticles inside each 100 nm radius liposome. Inter-nanoparticle distances were taken as 2, 6, and 10 times of SPIO nanoparticle radius to simulate different degree of aggregations. The root mean square (rms) angular frequency shift at the nanoparticle surface (compared to a point infinitely far away) was taken as $\Delta\omega_r = 1.7 \times 10^7$ rad/s. The diffusing water magnetizations were first positioned stochastically and the diffusion was modeled by random walks with periodic boundary conditions. The diffusion coefficient was taken as 2.3×10^{-9} m²/s for water at 25°C. In the simulation process, the effect of liposome membrane permeability was included as the probability of a diffusing water magnetization striking the liposome membrane to cross the barrier and enter inside the liposome. After each random-walk step, each water magnetization experienced a new, combined, net magnetic field, which was calculated by adding the dipolar fields from all the magnetic nanoparticles present. The Z-component of the induced dipolar field, $B_{dip,z}$, at position (d, θ) from the magnetic nanoparticle could be approximated by:

$$B_{dip,z}(d, \theta) = \sqrt{5/4} \frac{r^3 \Delta\omega_r}{\gamma d^3} (3 \cos^2 \theta - 1)$$

where γ is the gyromagnetic ratio of ^1H , r is the radius of the magnetic nanoparticle, $\Delta\omega_r$ is the root mean square (rms) angular frequency shift at the magnetic nanoparticle surface, d is the distance from the point to the center of the magnetic nanoparticle, and θ is the angle between the Z-axis and the position vector of the point.

Following an initial 90°_{xy} excitation pulse that flips all the equilibrium water magnetizations from +z to the +x direction, the time evolutions of 1000 diffusing water magnetizations were calculated by numerical integration of the Bloch equations [78] by Matlab (The MathWorks, Inc., Natick, MA, USA) using ordinary differential equation (ODE) solvers. As in the actual experiments, τ_{CP} in the CPMG pulse sequence was taken as 500 μ s. The average net water magnetization was calculated by averaging all the individual water magnetizations. The CPMG T_2 relaxation rate (R_2) was obtained by a linear fitting of the negative natural logarithm of the normalized transverse average water magnetization as a function of time.

Results and Discussions

Material characterization

The DLS results in PBS buffer provide an effective diameter of 231 nm for liposome nanoparticles with polydispersity index = 0.134. Intensity profile for size distribution has been shown in **Figure 2A**. It suggests that the nanoparticles are stable and well dispersed under biological condition at pH 7.4. DLS measurements were repeated after AMF heating and similar sizes (diameter = 223 nm \pm 1.6 nm) of liposome nanoparticles with polydispersity = 0.178 were obtained. Zeta potential of the liposome nanoparticles measured in water was found to be -12.63 mV. CryoTEM results are shown in the left and right panels of **Figure 2B** in different magnifications. They show homogeneous distribution and morphology of liposomes with embedded SPIO nanoparticles. Electron-dense objects, such as SPIO, appear as darker regions in the image. Larger aggregates of SPIO were visible as dark spots at this resolution. The magnified one in inset of the right panel demonstrates the encapsulation of SPIO nanoparticles inside the inner aqueous core of the liposomes. The Gd and Fe concentrations in the liposome solution were determined by ICP-OES to be 1.37 mM and 22.2 mM with \sim 5% uncertainty, respectively. Considering the unencapsulated 0.00382 mM Gd and 6.50 mM SPIO in the supernatant, the effective Fe and Gd concentrations in the liposome solution are 15.7 mM and 1.37 mM, respectively.

The synthesized liposomes with uniform size distribution (diameter \approx 200 nm) and low polydispersity ($<$ 0.2) indicate a homogeneous distribution in the solution. CryoTEM images demonstrate the successful encapsulation of SPIO nanoparticles inside the liposome nanoparticles.

The optimal size of the encapsulating liposome nanoparticle plays a key role in this kind of theranostic approach. Smaller size like less than 5 nm accelerates fast excretion through kidney filtration, while larger-size nanoparticles are easily recognized for uptake by reticuloendothelial system (RES). A size of around the inter-endothelial cell gap of a few hundred nanometers is considered as a key factor for the determination of optimal size, and previous studies have shown preferred size range is about 50-200 nm [79, 80] to reduce fast clearance and enhance passive tumor targeting by enhanced permeability and retention (EPR) effect [81].

SPIO-encapsulated liposomes are ideal candidates for magnetic targeting to the tumor and recent *in vivo* studies have shown the nanocarriers in the range of 200 nm could be efficiently targeted to the tumor by magnetofection [17, 72, 73]. In order to maximize the hyperthermia effect and magnetic targeting, a size of about 200 nm is generally preferred, as the magnetic force on the liposome would get enhanced in proportion to its size [17]. The association of polyethylene glycol (PEG) with the liposome nanoparticles is to increase the circulation time in blood for passive targeting by EPR. The unaltered size and polydispersity index before and after the AMF heating suggest that the liposome structure remained intact and the SPIO nanoparticles remained inside the liposome throughout the procedure. Additionally, the presence of SPIO nanoparticles inside the liposomes offers the nanovehicles active tumor targeting capability for superficial tumors by external magnetic force [72, 73]. Consequently, SPIO-encapsulated liposomes are structurally suitable to make nanoparticles biocompatible and offer a clinically proven, versatile platform for the further enhancement of pharmacological efficacy and targeting efficiency.

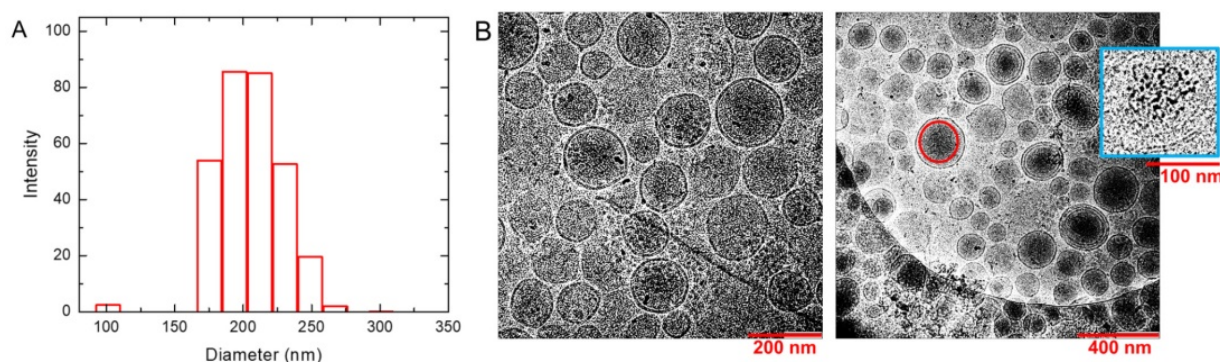


Figure 2. Characterization of liposomes. (A) Dynamic light scattering (DLS) of synthesized liposomes. It demonstrates the distribution of nanoparticles with an average diameter 231 nm and polydispersity 0.134. (B) CryoTEM images show the homogeneous distribution and morphology of liposomes in different magnifications. They show an average diameter around 200 nm and successful formation of bilayered spherical liposomes. The darker regions mark the presence of SPIO inside the liposome. A representative red circle is drawn to show such an SPIO concentrated region. The magnified liposome in blue box of the right panel shows the SPIO encapsulation inside the aqueous core of liposomes. Larger aggregates of SPIO appeared as darker spots.

AMF-controlled cargo (model drug fluorescein) release

The cargo release profile following AMF heating was monitored by using the self-quenching property of fluorescein [69, 71] that serves as a model for cancer drug, as it has the similar molecular size as the real cancer drug. The fluorescence yield is quenched depending on whether the fluorescein is inside the liposome with a high concentration or outside the liposome with a lower concentration. This property was used to quantify the percentage of fluorescein release from the liposome under AMF heating. All fluorescence measurements were performed after cooling the sample to room temperature following AMF heating. Although the measurements were performed up to a maximum bulk temperature of 39°C, the local temperatures inside liposomes could be higher than the bulk temperature by 15°C-20°C [82]. We have checked that the fluorescence properties remained unchanged up to 80°C by heating fluorescein up to 80°C in a water bath and then performing fluorescence experiments after cooling it to room temperature. No change in the spectral characteristics of fluorescein was seen in these experiments.

The characteristic cargo (fluorescein) release pattern as measured by fluorescence yield is shown by the dotted red curve in **Figure 3A**. We find from the dotted red curve in **Figure 3A** that the percentage of cargo release was initially low, and after a threshold, it increased at a faster rate and finally reached the maximum, indicating complete cargo release. The CryoTEM images in **Figure 2B** show that the number of SPIO nanoparticles in each liposomes varies, leading to the conjecture that the higher loaded liposomes released cargo at the beginning, and later on, other liposomes with

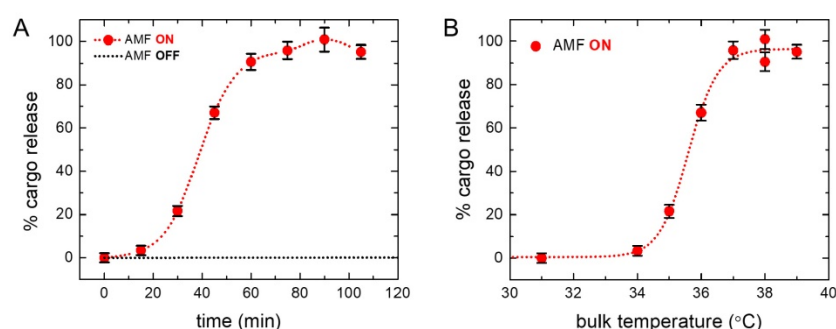


Figure 3. Cumulative cargo (fluorescein) release profile. (A) Cumulative cargo (fluorescein) release profile is shown as a function of the cumulative AMF heating time. Dotted red curve demonstrates the percentage of cargo release at different time. The characteristic pattern indicates the initial slow rate of release, then an increased rate of release between 30 to 45 minutes, and finally leveling off, indicating the complete release. Dotted black curve shows the spontaneous release of cargo from liposomes without AMF treatment and flat line depicts no leakage is observed otherwise. (B) Cumulative cargo (fluorescein) release profile is shown as a function of the maximum bulk temperature (before cooling to room temperature). Fluorescence measurements were performed at room temperature. It demonstrates that the maximum change in the bulk temperature during the process from no cargo release to complete release is about 3°C. The dotted lines through the data points are included in each case as a guide to the eye (see text for details).

average loading started to release cargo. **Figure 3A** and **Figure 3B** show experimental points for cumulative AMF heating time and corresponding maximum temperature of the bulk sample (before cooling). **Figure 3A** (dotted red curve) shows that the cargo release rate is fastest in the (30 - 45) minute time interval and levels off after an hour, indicating complete cargo release. However, the exact timing depends on the circumstantial set up and needs to be optimized, based on the clinical settings. A control liposome sample was measured before and after the treatment procedure to ensure that there was no leakage otherwise.

The dotted black line in **Figure 3A** represents the spontaneous cargo release profile of liposomes, which clearly shows cargo was not leaked without AMF heating. **Figure 3B** shows profile of the corresponding bulk temperature change with cargo release. The saturation temperature for the drug release is 37°C and the dramatic increase in the rate of drug release occurred between 34°C-37°C resulting in almost 100% drug release. AMF heating experiments show that significant percentage of drug release starts above 35°C and saturates at 37°C for this liposome. **Figure S1** in supplementary material shows a comparison of cargo release at different temperatures under AMF heating (red bar) and bulk heating in a bath (black bar). We find a significantly higher percentage of drug release at around 36°C under AMF heating, compared to that under the bulk bath heating. The choice of liposome provides the flexibility to easily manipulate the transition temperature by changing the lipid composition according to the clinical requirement [83].

Measuring local temperature inside the nanovehicle is challenging. However, there have been several methods to measure temperature inside the core of liposome by optical spectroscopy or using polymers [82, 84-87]. Ongoing effort in our labs is to develop theoretical methods to account for the aggregate formation and the size distribution of the magnetic nanoparticles inside the core of liposome to accurately estimate the specific loss power and heating efficiency for MR nanotheranostic hyperthermia in cancer therapy [35]. Based on those studies, generally speaking, higher the number of SPIO nanoparticles in the core of the liposome, more heat can be induced by the application of AMF.

Tracking MRI parameters

Figure 4A shows the percentage change of MRI parameter R_1 with the percentage of cargo release (dotted red line). We find a linear increase in the percentage of R_1 with the percentage of cargo release, and a maximum increase of R_1 is 69.8 %, indicates 100% cargo release. The results have been given in a tabular form in **Table 1**. This change in the R_1 value is attributed to the simultaneous release of Gd(III)-DTPA along with the model drug molecule fluorescein (cargo) from the liposome nanoparticles, since the presence of Gd(III)-DTPA outside the liposome would significantly increase the R_1 value of the water protons due to the free interaction of Gd(III) with the water protons, compared to those in the encapsulated state [34]. This hypothesis has been further confirmed by measuring the R_1 value of the liposome solution after completely lysing with Triton X-100, which provides the exact same value, as found from the maximum R_1 value after complete cargo release. It implies that the local heating increases the permeability of liposome membrane [88, 89], allowing leakage of both Gd(III)-DTPA and cargo,

and R_1 increases linearly with the cargo release. In order to further investigate the linear nature of the plot, we have fitted percentage changes in R_1 with percentage cargo (fluorescein) release in **Figure 4B** and obtained a linear equation (shown below) with squared correlation coefficient $R^2 = 0.997$.

$$\% \text{ Change in } R_1 = 0.686 \times (\% \text{ Change in cargo release})$$

Table 1. Data for percentage changes in MR relaxation rates with different percentage of cargo (fluorescein) release

% Cargo (fluorescein) release ^a	% R_1 change ^b	% R_2 change ^b
0	0	0
1.194	-0.482	-1.746
6.202	4.373	-7.548
69.449	46.935	-1.766
85.559	58.833	-2.195
95.228	69.904	0.272
101.739	65.780	-1.878

^aStandard deviation is 3 %. ^bStandard deviation is 0.3 %. R_1 : Longitudinal relaxation rate, R_2 : Transverse relaxation rate, MR: Magnetic resonance

The black curve in **Figure 4A** shows the percentage change of R_2 , which remains essentially constant, independent of cargo release (data are

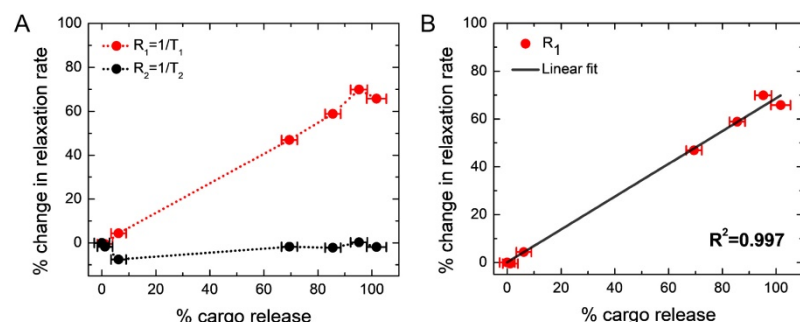


Figure 4. Correlation between changes in MR relaxation rates and cargo (fluorescein) release. **(A)** Red curve indicates the percentage change in R_1 and black curve indicates the percentage change in R_2 . It demonstrates R_1 linearly increases with cargo release, and shows maxima after 69.8% increase, when cargo release was complete. R_2 is held nearly constant; however, it shows an initial 7%-drop (from the second to the third point, corresponding to the path of no cargo release to about 6% cargo release) and then a gradual increase to the initial value. Please see the text for the plausible explanation. The dotted lines through the data points are included in each case as a guide to the eye. **(B)** Fitted linear plot for percentage change in longitudinal relaxation rate (R_1) with percentage cargo (fluorescein) release. The fitted linear equation: % Change in $R_1 = 0.686 \times$ (% Change in cargo release) with squared correlation coefficient $R^2 = 0.997$.

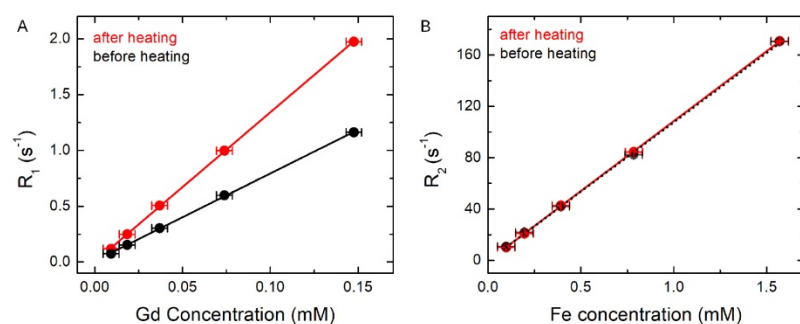


Figure 5. MR relaxation rates were measured at different dilutions before and after complete AMF heating. **(A)** R_1 versus Gd concentration before and after complete AMF heating. It shows the slope of the fitted linear plot before (black) $r_1 = 7.84 \text{ s}^{-1} \text{ mM}^{-1}$ (Gd) and after complete AMF heating (red) $r_1 = 13.38 \text{ s}^{-1} \text{ mM}^{-1}$ (Gd). **(B)** R_2 versus Fe concentration before and after complete AMF heating. It shows the slope of the fitted linear plot before (black) $r_2 = 108.01 \text{ s}^{-1} \text{ mM}^{-1}$ (Fe) and after complete AMF heating (red) $r_2 = 108.93 \text{ s}^{-1} \text{ mM}^{-1}$ (Fe). The uncertainties on R_1 and R_2 are $< 1\%$, whereas the uncertainties on the concentration are $\sim 5\%$.

shown in **Table 1**). However, a closer look reveals that initially (along second to third point in the black curve in **Figure 4A**, corresponding to the path of no cargo release to about 6% cargo release or the 3rd point in **Table 1**) it dropped by about 7% and later it increased back to the initial value. DLS measurements did not show any significant change of the size of liposomes as a result of mild AMF heating. On the other hand, R_2 parameter of the completely lysed sample (where all the SPIO nanoparticles should be outside the liposome encapsulation) was found to be reduced by $\approx 20\%$, compared to that in the pretreated sample (data not shown). Hence, mild AMF heating is not causing any significant leakage of SPIO nanoparticles from the liposome encapsulation, as also concluded in earlier work [44]. Since SPIO particles remained inside liposome during AMF heating and the liposome could be attached to the tumor site, the encapsulated SPIO particles could be used for online monitoring of the tumor site. Our theoretical simulations provide a qualitative explanation of the initial small drop and later slight increase of R_2 under mild AMF heating (**Figure 4A**), as discussed in the next section.

In order to further understand and quantify the changes of the relaxation rates, R_1 and R_2 , relaxivities (r_1 and r_2) were determined by measuring the relaxation rates at different dilutions both before and after complete AMF heating. In **Figure 5A**, black and red lines show R_1 versus Gd concentration plots before and after complete AMF heating, respectively. The slope of the black line (before AMF heating) is $r_1 = 7.84 \text{ s}^{-1} \text{ mM}^{-1}$, while the slope of the red line (after AMF heating) is $r_1 = 13.38 \text{ s}^{-1} \text{ mM}^{-1}$. In **Figure 5B**, we show the plots of R_2 versus Fe concentration both before (in black) and after (in red) complete AMF heating. It shows that the slopes of the red and black lines are $r_2 = 108.93 \text{ s}^{-1} \text{ mM}^{-1}$ and $108.01 \text{ s}^{-1} \text{ mM}^{-1}$, respectively, *i.e.* they are about equal. It is clear from the plots that AMF heating significantly affects the R_1 versus Gd concentration curve and increases r_1 of the AMF-treated sample by $\approx 70\%$, whereas the heating has almost no effect on the R_2 versus Fe concentration curve. Furthermore, the complete linear nature of the plots in **Figure 5** confirms that the changes in longitudinal relaxation rates, R_1 , are mainly affected by Gd or Gd(III)-DTPA concentration, and changes in transverse relaxation rates, R_2 , are associated with Fe or SPIO concentration.

Monte Carlo spin dynamics simulations

Figure 6A shows the effect of liposome membrane permeability on R_2 for different inter-nanoparticle distances (D_{pp}) of the SPIO aggregates. Here, we define water permeability as the probability of a diffusing water magnetization striking the liposome membrane to cross the barrier and enter inside the liposome. We have plotted membrane permeability versus R_2 for different values of D_{pp}/r_p (where r_p is the radius of a SPIO nanoparticle). Higher D_{pp} indicates weaker aggregation state of SPIO and smaller D_{pp} implies stronger aggregation state. We find from **Figure 6A** that the nature of variation of R_2 with permeability

is qualitatively independent of D_{pp}/r_p . R_2 increases sharply with permeability from $1 \times 10^{-3}\%$ to 0.1% and saturates for permeability $> 0.1\%$. Thus, even a small change in liposome membrane permeability in the range ($1 \times 10^{-3}\%$ to 0.1%) would result in a significant increase of R_2 . As permeability increases, the water molecules are more likely to diffuse closer to the SPIO nanoparticles encapsulated inside the liposome and exchange faster with the "fresh" water magnetization outside the liposome, thus experiencing stronger fluctuating magnetic fields and resulting in a higher R_2 value, as seen in **Figure 6A**. **Figure 6B** shows the correlation between R_2 and D_{pp}/r_p for different liposome membrane permeabilities. We find that the liposome membrane with permeability higher than $1 \times 10^{-3}\%$ exhibits a significant drop in R_2 value with higher D_{pp} . However, the liposomes with membrane permeability less than $1 \times 10^{-3}\%$ do not show noticeable change in R_2 for different aggregation status. The diffusing water magnetizations experience stronger dipolar magnetic fields when SPIO is in stronger aggregation state, compared to those in the weaker aggregation state where the resulting net SPIO dipolar field experienced by diffusing water magnetizations is partially cancelled out by individual fields [44, 54].

We have estimated the chance of a diffusing water magnetization passing through the intact liposome membrane per collision would be between 1×10^{-5} and 1×10^{-4} (or 0.001% - 0.01%) in normal condition [90, 91], taking the thickness of liposome membrane $\approx 3 \text{ nm}$ and the water permeability $10^{-1.95} \text{ cm/s}$. Liposome membrane undergoes reversible permeability change on heating [88, 89], and this change is significantly higher near the phospholipid phase transition temperature of $\approx 41^\circ\text{C}$ [44]. In this experiment, we did the heating close to its transition temperature, leading to the possibility of significant permeability change of the synthesized thermosensitive liposome membrane. However, the

R_2 measurements were done after cooling the sample to room temperature. Since the permeability change should be mostly reversible initially under mild heating, we do not expect any significant increase of the measured R_2 due to the change of membrane permeability at the initial stage. On the other hand, during the process of AMF heating, as the membrane permeability would increase, there would be higher access of water molecules inside the liposome, thus increasing D_{pp} and causing disaggregate of SPIO clusters. This change of the SPIO aggregation state inside liposome should be retained when the solution

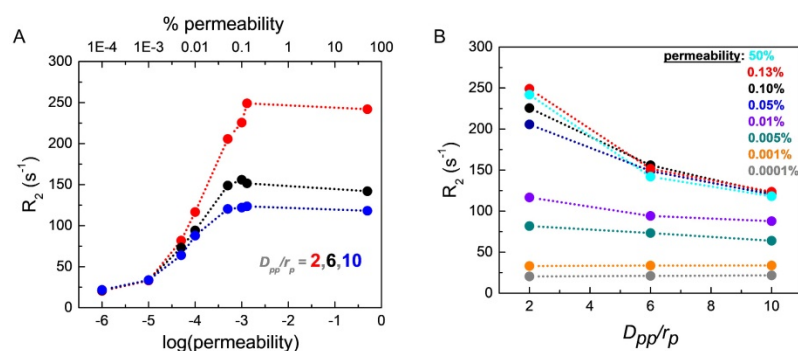


Figure 6. The effects of liposome membrane permeability and SPIO aggregation inside liposome on CPMG R_2 relaxation rates. (A) CPMG relaxation rates R_2 are plotted as a function of the liposome membrane permeability at three different aggregation states with D_{pp} (inter-SPIO nanoparticle distance) / r_p (single SPIO radius) = 2, 6, and 10, respectively. The radius of a single SPIO, $r_p = 5 \text{ nm}$. **(B)** CPMG relaxation rates R_2 are plotted as a function of the degree of aggregation, D_{pp}/r_p , at different liposome membrane permeability conditions. The dotted lines through the points are included in each case as a guide to the eye.

was cooled back to room temperature and cause a slight decrease of R_2 value initially. As the heating process would continue repeatedly, the change in the liposome membrane permeability might not be completely reversible when cooled back to room temperature, causing R_2 value to rise. The interplay of these two opposing effects explains the observed initial small drop in R_2 and a subsequent slight increase, as seen in **Figure 4A** (black curve).

On the other hand, unencapsulated SPIO nanoparticles would be dispersed uniformly in the solution. Only a very small fraction can form aggregates under thermal equilibrium and the average value of D_{pp}/r_p is expected to be higher for such aggregates in the absence of any physical constraints like liposome membrane to ensure that they remain close to one another. Hence, R_2 value should decrease if all the SPIO nanoparticles would come out from the liposome enclosure as a result of lysing with Triton X-100. Experimentally, we have observed $\approx 20\%$ decrease in the R_2 value after lysing with Triton X-100 (data not shown) and this decrease is much higher than the initial 7%-drop in R_2 due to mild AMF heating. Since **Figure 4A** does not show any large drop ($\approx 20\%$) in the R_2 value, we conclude that SPIO nanoparticles remain within the liposome enclosure during the mild AMF heating process.

We performed R_2 measurements at room temperature after cooling the sample, when the liposome membrane property should be largely restored. However, our simulation results (**Figure 6A**) predict a sharp increase in R_2 with small increase of the liposome membrane permeability. Therefore, we expect to observe significant increase in R_2 for *in situ* MRI measurements with AMF heating. Since liposome could be efficiently functionalized to target the tumor site [16, 74], such *in situ* real-time MRI measurements with AMF heating opens up the possibility of high-resolution, high-contrast imaging of the tumor site during the MR theranostic process because of the large R_2 values.

In principle, the r_1 and r_2 relaxivities in spin systems with magnetic nanoparticles increase with temperature [92], as both diffusion of the water ^1H spins and nanoparticle cluster size increase with temperature [35]. In our current study, however, such temperature-dependent effect may be ignored compared with the dominating permeability-dependent effect, due to the small temperature range used under mild hyperthermia condition and the fact that the magnetic nanoparticles are encapsulated inside the core of the liposome. On the other hand, the liposome membrane permeability changes significantly over the mild-hyperthermia temperature range, as the temperature above which the fluorescein drug release rate from this liposome increases rapidly is about 35°C (**Figure 3B**),

although the phospholipid phase transition temperature for this liposome is 41°C [44].

Future scope and application

Compared to the previous studies done by Bos and coworkers [44], we have used liposomes with similar compositions; moreover, we have incorporated a model cancer drug fluorescein to study controlled dose release at target site. Furthermore, we have used AMF controlled delivery, which safely allows deeper penetration inside human body compared to HIFU and increases the scope of treatment. Earlier studies [37, 55] have shown that encapsulation of cancer drug inside temperature sensitive liposome increases tumor drug concentrations and improve antitumor efficacy of the drugs. The studies have shown 2-4 fold [40] and 2-16 fold [93] increase compared to non-heated condition, respectively. We have used a similar PEGylated temperature sensitive liposome and shown AMF controlled heating mechanism in relation to dosage delivery and carefully characterized MR relaxation parameters by encapsulating contrast agents at the same time. Hence, our study successfully extends previous studies to MR cancer theranostics. Moreover, at higher temperature, the permeability of liposome membrane increases. The simulations show that R_2 parameter increases rapidly with the permeability of the liposome membrane, raising the possibility of getting high-quality MRI images, if MR measurements could be done during AMF heating at the elevated temperature.

In this study, we have used cargo fluorescein as a model cancer drug and established a detailed correlation between the magnetic heating stimulated cargo releases with MR relaxation parameters through experimental study and theoretical understanding. Previous extensive studies were done [75, 76, 94] to understand the rate of release of real cancer drugs at *in vitro* and *in vivo* conditions and the results have been well understood by different diffusion- and dissolution-based mathematical models (squared correlation coefficient near 1), such as the Reciprocal Powered Time (RPT) or Weibull (W) model [75, 76]. Authors [76] found that *in vitro* and *in vivo* data could be best fitted in the RPT model, which is based on the general equation of dissolution and diffusion rate limited process $dw/dt = (D/h) \times S \times C_s$ under sink condition, where dw/dt is the rate of drug release, D is the drug molecule diffusion coefficient, S is the effective surface area of drug with release medium, C_s is solubility of the drug, and h is the length of diffusion path. Other studies found a good linear correlation between drug release in *in vitro* experiments with the drug absorption in *in vivo* experiments [75]. Hence, it is clear that the rate of real cancer drug release primarily depends on

diffusion and solubility. The diffusion coefficient depends on the hydrodynamic size of the drug molecule. It is well known that the hydrodynamic size of fluorescein is similar to many cancer drug molecules and therefore fluorescein was used as a model cancer drug in a large number of previous studies [48, 69–71].

Another important factor comes from the solubility of the drug, which depends on its particular nature, bonding, and hydrophobicity. For the poorly soluble cancer drugs, rate of release would be slower and, accordingly, AMF time could be adjusted depending on the exact clinical situation. However, the probability of encapsulation of a molecule in liposome is also proportional to the solubility of the molecule in the medium, and hence correspondingly fewer cancer drug molecules would be encapsulated. As a result, the AMF driven percentage release of drug, *i.e.*, $[(dw/dt)/w * 100]$, through diffusion of encapsulated molecule with different solubility would be similar. Hence, we expect qualitatively similar results for both model drug fluorescein and real cancer drug in *in vitro* or *in vivo* conditions, when the results are plotted as the percentage of drug release. Simultaneous release of Gd(III)-DTPA and fluorescein or the changes in aggregation status of SPIO are expected to remain unaltered for *in vivo* situation. Thus, the observed linear correlation between percentage drug release versus the percentage increase in R_1 can also be expected for real cancer drugs in clinical conditions, because the drug release process is essentially a diffusion process through a membrane. Similarly, the characteristic pattern of percentage changes in R_2 as a function of the percentage release of encapsulated drug would remain qualitatively the same for real cancer drugs in clinical condition. However, if the real drug would interact with the membrane of liposome or the process would not be diffusion, the results could be different. Nevertheless, for a large class of commonly used cancer drugs, the diffusion model holds and our results should remain valid for real cancer drugs in clinical conditions.

In this proof-of-concept study, we have focused on temperature effect on drug release. In a mild hyperthermia, blood perfusion and tumor oxygenation pattern change inhomogeneously and this change in local environment is very crucial for planning an effective treatment protocol. Various bioheat equations, tissue parameters, and temperature details should be taken into account to estimate tumor perfusion and changes in tumor local environment after employing mild heating. In this regard, many theoretical modeling and experiments were done [95–97] with real tumor. Future *in vivo* and clinical studies are required in this regard to implement the technique for clinical application. Systematic measurements of the drug release after

heating with distinct temperature and time using a water bath and using AMF, respectively, would provide insights to the heating mechanism and the interplay between the local temperature and the bulk temperature.

Conclusions

Real-time visualization of nano-drug carrier biodistributions, drug release processes, and therapeutic responses could provide critical information to dynamically optimize treatment operations in precision medicine in real time. In this work, we have demonstrated a novel MR theranostic approach that could be combined with the established targeting capacity of liposomes to deliver and release cargo with spatial control by AMF heating and simultaneously monitor both the cargo release and condition of the liposomal sites. We have used appropriate size of liposome nanoparticles and shown that the cargo release from the liposomes by AMF controlled mild hyperthermia could be quantified by measuring the longitudinal relaxation rate, R_1 . We have confirmed that SPIO remained inside the liposome enclosure during AMF heating by observing that R_2 remained approximately constant during the heating process. Monte Carlo spin dynamics simulations provided qualitative explanations to the observed variations in R_2 during the AMF heating process and predicted a sharp increase in R_2 due to a small increase in the liposome membrane permeability. The simulation results imply that real-time, *in-situ* MRI measurements with AMF heating could provide high-resolution, high-contrast image of the liposomal site during the heating process.

In conclusion, this work provides a proof of concept for monitoring cargo (cancer drugs) release with dosage control and liposomal site simultaneously by MRI technique. We have used clinically approved materials such as liposome, SPIO, and Gd(III)-DTPA in our experiments to accelerate the chance of getting readily accepted for pre-clinical or translational MR theranostics. Future work should be done *in vivo* with real drug molecules, with active targeting by magnetofection, and with real-time, *in-situ* MRI measurements and AMF heating.

Abbreviations

AMF: alternating magnetic field; BBB: blood brain barrier; cryoTEM: transmission electron cryo-microscopy; DLS: dynamic light scattering; D_{pp} : inter SPIO nanoparticle distance; EPR: enhanced permeability and retention; Fe: iron; Gd: Gadolinium; Gd(III)-DTPA: diethylenetriaminepentaacetic acid gadolinium(III); HIFU: high intensity focused ultrasound; ICP-OES: inductively coupled plasma optical emission spectrometry; MRI: magnetic resonance imaging; NMR: nuclear magnetic

resonance; PBS: phosphate buffered saline; PEG: polyethylene glycol; R_1 : longitudinal relaxation rate; r_1 : longitudinal relaxivity; R_2 : transverse relaxation rate; r_p : single SPIO radius; r_2 : transverse relaxivity; RES: reticuloendothelial system; RPT: Reciprocal Powered Time; SPIO: superparamagnetic iron oxide; τ_{CP} : half of the interval between successive 180° pulses in a CPMG sequence.

Acknowledgements

We gratefully acknowledge Mr. Ivo Atanasov, Dr. Peng Ge, Dr. Christian Beren for technical support and Prof. William Gelbart, Prof. Charles M. Knobler, Prof. Neil K. Garg, Prof. Andre Nel for lab facility. This work was supported by National Science Foundation (CHE-1112574, CHE-1416598), University of California Cancer Research Award (CRR-13-201412), and the Hirshberg Foundation for Pancreatic Cancer Research (YYL, ZL).

Supplementary Material

Supplementary figure.

<http://www.ntno.org/v03p0166s1.pdf>

Competing Interests

The authors have declared that no competing interest exists.

References

- Kelkar SS, Reineke TM. Theranostics: combining imaging and therapy. *Bioconjug. Chem.* 2011; 22: 1879–1903
- Wang H, Li X, Tse BW-C et al. Indocyanine green-incorporating nanoparticles for cancer theranostics. *Theranostics* 2018; 8: 1227–1242
- Janib SM, Moses AS, MacKay JA. Imaging and drug delivery using theranostic nanoparticles. *Adv. Drug Deliv. Rev.* 2010; 62: 1052–1063
- Wang J, Liu L, You Q et al. All-in-one theranostic nanoplatfrom based on hollow MoS₂ for photothermally-manuevered oxygen self-enriched photodynamic therapy. *Theranostics* 2018; 8: 955–971
- Sunderland CJ, Steiert M, Talmadge JE et al. Targeted nanoparticles for detecting and treating cancer. *Drug Dev. Res.* 2006; 67: 70–93
- Tan J, Yang N, Zhong L et al. A new theranostic system based on endoglin aptamer conjugated fluorescent silica nanoparticles. *Theranostics* 2017; 7: 4862–4876
- Singh R, Lillard JW. Nanoparticle-based targeted drug delivery. *Exp. Mol. Pathol.* 2009; 86: 215–223
- Brannon-Peppas L, Blanchette JO. Nanoparticle and targeted systems for cancer therapy. *Adv. Drug Deliv. Rev.* 2012; 64: 206–212
- Parekh G, Shi Y, Zheng J et al. Nano-carriers for targeted delivery and biomedical imaging enhancement. *Ther. Deliv.* 2018; 9: 451–468
- Hekman MC, Rijpkema M, Muselaers CH et al. Tumor-targeted dual-modality imaging to improve intraoperative visualization of clear cell renal cell carcinoma: a first in man study. *Theranostics* 2018; 8: 2161–2170
- Ashton JR, Castle KD, Qi Y et al. Dual-energy CT imaging of tumor liposome delivery after gold nanoparticle-augmented radiation therapy. *Theranostics* 2018; 8: 1782–1797
- Kong X, Dong B, Song X et al. Dual turn-on fluorescence signal-based controlled release system for real-time monitoring of drug release dynamics in living cells and tumor tissues. *Theranostics* 2018; 8: 800–811
- Slowing II, Vivero-Escoto JL, Wu C-W et al. Mesoporous silica nanoparticles as controlled release drug delivery and gene transfection carriers. *Adv. Drug Deliv. Rev.* 2008; 60: 1278–1288
- Kotb S, Detappe A, Lux F et al. Gadolinium-based nanoparticles and radiation therapy for multiple brain melanoma metastases: Proof of concept before phase I trial. *Theranostics* 2016; 6: 418–427
- Yen SK, Padmanabhan P, Selvan ST. Multifunctional iron oxide nanoparticles for diagnostics, therapy and macromolecule delivery. *Theranostics* 2013; 3: 986–1003
- Hosta-Rigau L, Schattling P, Teo BM et al. Recent progress of liposomes in nanomedicine. *J. Mater. Chem. B* 2014; 2: 6686–6691
- Béalle G, Di Corato R, Kolosnjaj-Tabi J et al. Ultra magnetic liposomes for MR imaging, targeting, and hyperthermia. *Langmuir* 2012; 28: 11834–11842
- Pradhan P, Giri J, Rieken F et al. Targeted temperature sensitive magnetic liposomes for thermo-chemotherapy. *J. Control. Release* 2010; 142: 108–121
- Mikhaylov G, Mikac U, Magaeva AA et al. Ferri-liposomes as an MRI-visible drug-delivery system for targeting tumours and their microenvironment. *Nat. Nanotechnol.* 2011; 6: 594–602
- Amstad E, Kohlbrecher J, Müller E et al. Triggered release from liposomes through magnetic actuation of iron oxide nanoparticle containing membranes. *Nano Lett.* 2011; 11: 1664–1670
- Zhang L, Cui H. HAase-sensitive dual-targeting irinotecan liposomes enhance the therapeutic efficacy of lung cancer in animals. *Nanotheranostics* 2018; 2: 280–294
- Knights-Mitchell SS, Romanowski M. Near-infrared activated release of doxorubicin from plasmon resonant liposomes. *Nanotheranostics* 2018; 2: 295–305
- Koning GA, Eggermont AMM, Lindner LH et al. Hyperthermia and thermosensitive liposomes for improved delivery of chemotherapeutic drugs to solid tumors. *Pharm. Res.* 2010; 27: 1750–1754
- Allen TM, Cullis PR. Liposomal drug delivery systems: from concept to clinical applications. *Adv. Drug Deliv. Rev.* 2013; 65: 36–48
- Meunier F, Prentice HG, Ringden O. Liposomal amphotericin B (AmBisome): safety data from a phase II/III clinical trial. *J. Antimicrob. Chemother.* 1991; 28: 83–91
- Morris PE, Papadakos P, Russell JA et al. A double-blind placebo-controlled study to evaluate the safety and efficacy of L-2-oxothiazolidine-4-carboxylic acid in the treatment of patients with acute respiratory distress syndrome. *Crit. Care Med.* 2008; 36: 782–788
- Rahman A, Treat J, Roh JK et al. A phase I clinical trial and pharmacokinetic evaluation of liposome-encapsulated doxorubicin. *J. Clin. Oncol.* 1990; 8: 1093–1100
- Delanian S, Baillet F, Huart J et al. Successful treatment of radiation-induced fibrosis using liposomal CuZn superoxide dismutase: clinical trial. *Radiother. Oncol.* 1994; 32: 12–20
- Hortobagyi GN, Ueno NT, Xia W et al. Cationic liposome-mediated E1A gene transfer to human breast and ovarian cancer cells and its biologic effects: a phase I clinical trial. *J. Clin. Oncol.* 2001; 19: 3422–3433
- Northfelt DW, Dezube BJ, Thommes JA et al. Pegylated-liposomal doxorubicin versus doxorubicin, bleomycin, and vincristine in the treatment of AIDS-related Kaposi's sarcoma: results of a randomized phase III clinical trial. *J. Clin. Oncol.* 1998; 16: 2445–2451
- Alberts DS, Muggia FM, Carmichael J et al. Efficacy and safety of liposomal anthracyclines in Phase I/II clinical trials. *Semin. Oncol.* 2004; 31: 53–90
- Field SB, Bleehen NM. Hyperthermia in the treatment of cancer. *Cancer Treat. Rev.* 1979; 6: 63–94
- Wust P, Hildebrandt B, Sreenivasa G et al. Hyperthermia in combined treatment of cancer. *Lancet Oncol.* 2002; 3: 487–497
- Tagami T, Foltz WD, Ernsting MJ et al. MRI monitoring of intratumoral drug delivery and prediction of the therapeutic effect with a multifunctional thermosensitive liposome. *Biomaterials* 2011; 32: 6570–6578
- Wang C, Hsu CH, Li Z et al. Effective heating of magnetic nanoparticle aggregates for in vivo nano-theranostic hyperthermia. *Int. J. Nanomedicine* 2017; 12: 6273–6287
- Clavel CM, Nowak-Sliwinska P, Păunescu E et al. In vivo evaluation of small-molecule thermoresponsive anticancer drugs potentiated by hyperthermia. *Chem. Sci.* 2015; 6: 2795–2801
- Ponce AM, Vujaskovic Z, Yuan F et al. Hyperthermia mediated liposomal drug delivery. *Int. J. Hypertherm.* 2006; 22: 205–213
- Unezaki S, Maruyama K, Takahashi N et al. Enhanced delivery and antitumor activity of doxorubicin using long-circulating thermosensitive liposomes containing amphiphatic polyethylene glycol in combination with local hyperthermia. *Pharm. Res.* 1994; 11: 1180–1185
- Needham D, Anyarambhatla G, Kong G et al. A new temperature-sensitive liposome for use with mild hyperthermia: characterization and testing in a human tumor xenograft model. *Cancer Res.* 2000; 60: 1197–1201
- Kong G, Braun RD, Dewhirst MW et al. Hyperthermia enables tumor-specific nanoparticle delivery: effect of particle size. *Cancer Res.* 2000; 60: 4440–4445
- Lin FC, Hsu CH, Lin YY. Nano-therapeutic cancer immunotherapy using hyperthermia-induced heat shock proteins: insights from mathematical modeling. *Int. J. Nanomedicine* 2018; 13: 1–11
- Boissenot T, Bordat A, Fattal E et al. Ultrasound-triggered drug delivery for cancer treatment using drug delivery systems: from theoretical considerations to practical applications. *J. Control. Release* 2016; 241: 144–163
- Ranjan A, Jacobs GC, Woods DL et al. Image-guided drug delivery with magnetic resonance guided high intensity focused ultrasound and temperature sensitive liposomes in a rabbit Vx2 tumor model. *J. Control. Release* 2012; 158: 487–494
- Lorenzato C, Oerlemans C, van Elk M et al. MRI monitoring of nanocarrier accumulation and release using Gadolinium-SPIO co-labelled thermosensitive liposomes. *Contrast Media Mol. Imaging* 2016; 11: 184–194
- Tai LA, Tsai PJ, Wang YC et al. Thermosensitive liposomes entrapping iron oxide nanoparticles for controllable drug release. *Nanotechnology* 2009; 20: 135101
- Thomas CR, Ferris DP, Lee J et al. Noninvasive remote controlled release of drug molecules in vitro using magnetic actuation of mechanised nanoparticles. *J. Am. Chem. Soc.* 2010; 132: 10623–10625
- Saint-Cricq P, Deshayes S, Zink JI et al. Magnetic field activated drug delivery using thermodegradable azo-functionalised PEG-coated core-shell mesoporous silica nanoparticles. *Nanoscale* 2015; 7: 13168–13172
- Rühle B, Datz S, Argyo C et al. A molecular nanocap activated by superparamagnetic heating for externally stimulated cargo release. *Chem. Commun.* 2016; 52: 1843–1846

49. Banks WA, Gray AM, Erickson MA et al. Alternating magnetic field-induced hyperthermia increases iron oxide nanoparticle cell association/uptake and flux in blood– brain barrier models. *Pharm. Res.* 2015; 32: 1615–1625
50. Song X, Han X, Yu F et al. Polyamine-targeting gefitinib prodrug and its near-infrared fluorescent theranostic derivative for monitoring drug delivery and lung cancer therapy. *Theranostics* 2018; 8: 2217–2228
51. Li X, Schumann C, Albarqi HA et al. A tumor-activatable theranostic nanomedicine platform for NIR fluorescence-guided surgery and combinatorial phototherapy. *Theranostics* 2018; 8: 767–784
52. Langereis S, Hijnen N, Strijkers G et al. Research spotlight: multifunctional liposomes for MRI and image-guided drug delivery. *Ther. Deliv.* 2014; 5: 21–24
53. Ho LC, Hsu CH, Ou CM et al. Unibody core-shell smart polymer as a theranostic nanoparticle for drug delivery and MR imaging. *Biomaterials* 2015; 37: 436–446
54. Lorenzato C, Cernicanu A, Meyre ME et al. MRI contrast variation of thermosensitive magnetoliposomes triggered by focused ultrasound: A tool for image-guided local drug delivery. *Contrast Media Mol. Imaging* 2013; 8: 185–192
55. Ponce AM, Viglianti BL, Yu D et al. Magnetic Resonance imaging of temperature-sensitive liposome release: drug dose painting and antitumor effects. *JNCI J. Natl. Cancer Inst.* 2007; 99: 53–63
56. Talanov VS, Regino CAS, Kobayashi H et al. Dendrimer-based nanoprobe for dual modality magnetic resonance and fluorescence imaging. *Nano Lett.* 2006; 6: 1459–1463
57. Wen S, Li K, Cai H et al. Multifunctional dendrimer-entrapped gold nanoparticles for dual mode CT/MR imaging applications. *Biomaterials* 2013; 34: 1570–1580
58. Luo Y, Zhao L, Li X et al. The design of a multifunctional dendrimer-based nanoplatform for targeted dual mode SPECT/MR imaging of tumors. *J. Mater. Chem. B* 2016; 4: 7220–7225
59. Haribabu V, Farook AS, Goswami N et al. Optimized Mn-doped iron oxide nanoparticles entrapped in dendrimer for dual contrasting role in MRI. *J. Biomed. Mater. Res. - Part B Appl. Biomater.* 2016; 104: 817–824
60. Szpak A, Fiejdasz S, Prendota W et al. T1-T2 Dual-modal MRI contrast agents based on superparamagnetic iron oxide nanoparticles with surface attached gadolinium complexes. *J. Nanoparticle Res.* 2014; 16: 1–11
61. Zhou Z, Huang D, Bao J et al. A synergistically enhanced $T_1 - T_2$ Dual-modal contrast agent. *Adv. Mater.* 2012; 24: 6223–6228
62. Hu F, Zhao YS. Inorganic nanoparticle-based T1 and T1/T2 magnetic resonance contrast probes. *Nanoscale* 2012; 4: 6235–6243
63. Jung H, Park B, Lee C et al. Dual MRI T1 and T2(*) contrast with size-controlled iron oxide nanoparticles. *Nanomedicine Nanotechnology, Biol. Med.* 2014; 10: 1679–1689
64. Soenen SJH, Desender L, De Cuyper M. Complexation of gadolinium(III) ions on top of nanometre-sized magnetoliposomes. *Int. J. Environ. Anal. Chem.* 2007; 87: 783–796
65. Shin T, Choi J, Yun S et al. T1 and T2 dual-mode MRI contrast agent for enhancing accuracy by engineered nanomaterials. *ACS Nano* 2014; 8: 3393–3401
66. Estelrich J, Sánchez-Martín MJ, Busquets MA. Nanoparticles in magnetic resonance imaging: From simple to dual contrast agents. *Int. J. Nanomedicine* 2015; 10: 1727–1741
67. De Cuyper M, Soenen SJH, Coenegrachts K et al. Surface functionalization of magnetoliposomes in view of improving iron oxide-based magnetic resonance imaging contrast agents: anchoring of gadolinium ions to a lipophilic chelate. *Anal. Biochem.* 2007; 367: 266–273
68. Chen J, Zhang WJ, Guo Z et al. PH-responsive iron manganese silicate nanoparticles as T1- T2* dual-modal imaging probes for tumor diagnosis. *ACS Appl. Mater. Interfaces* 2015; 7: 5373–5383
69. Huang HL, Lu PH, Yang HC et al. Fiber-optic triggered release of liposome in vivo: Implication of personalized chemotherapy. *Int. J. Nanomedicine* 2015; 10: 5171–5185
70. Paris JL, Cabañas MV, Manzano M et al. Polymer-grafted mesoporous silica nanoparticles as ultrasound-responsive drug carriers. *ACS Nano* 2015; 9: 11023–11033
71. Niesman MR, Khoobehi B, Peyman GA. Encapsulation of sodium fluorescein for dye release studies. *Investig. Ophthalmol. Vis. Sci.* 1992; 33: 2113–2119
72. Al-Jamal KT, Bai J, Wang JT-W et al. Magnetic drug targeting: preclinical in vivo studies, mathematical modeling, and extrapolation to humans. *Nano Lett.* 2016; 16: 5652–5660
73. T-w J, Bai J, T-W Wang J et al. Triple-modal imaging of magnetically-targeted nanocapsules in solid tumours in vivo. *Theranostics* 2016; 6: 342–356
74. Takeda K, Kobari M, Akaishi S et al. Targeting pancreatic chemotherapy cancer using liposome against antibody-combined. *J. Exp. Med.* 1994; 175: 29–42
75. D'Souza S. A review of in vitro drug release test methods for nano-sized dosage forms. *Adv. Pharm.* 2014; 2014: 1–12
76. Barzegar-Jalali M, Adibkia K, Valizadeh H et al. Kinetic analysis of drug release from nanoparticles. *J. Pharm. Pharm. Sci.* 2008; 11: 167–177
77. Beren CE. Effect of secondary structure on the size, configurational statistics, and packaging of long-RNA by viral capsid protein. Abstract of dissertation 2017
78. Liang ZP, Lauterbur PC. Principles of magnetic resonance imaging: a signal processing perspective. *IEEE Engineering in Medicine and Biology Society, New York, US: SPIE Optical Engineering Press; 2000*
79. Nel A, Ruoslahti E, Meng H. New insights into "permeability" as in the enhanced permeability and retention effect of cancer nanotherapeutics. *ACS Nano* 2017; 11: 9567–9569
80. Fang J, Nakamura H, Maeda H. The EPR effect: Unique features of tumor blood vessels for drug delivery, factors involved, and limitations and augmentation of the effect. *Adv. Drug Deliv. Rev.* 2011; 63: 136–151
81. Merbach A, Helm L, Tóth E et al. The chemistry of contrast agents in medical magnetic resonance imaging, 2nd ed. Chichester, UK: Wiley; 2013
82. Dong J, Zink JI. Taking the temperature of the interiors of magnetically heated nanoparticles. *ACS Nano* 2014; 8: 5199–5207
83. Yang C, City T. (19) United States (12) Patent Application Publication (10) Pub. No.: US 2009 / 0004258 A1 I05. 2009; 1
84. Vetrone F, Naccache R, Zamarrón A et al. Temperature sensing using fluorescent nanothermometers. *ACS Nano* 2010; 4: 3254–3258
85. Ye F, Wu C, Jin Y et al. Ratiometric temperature sensing with semiconducting polymer dots. *J. Am. Chem. Soc.* 2011; 133: 8146–8149
86. Freddi S, Sironi L, D'Antuono R et al. A molecular thermometer for nanoparticles for optical hyperthermia. *Nano Lett.* 2013; 13: 2004–2010
87. Polo-Corrales L, Rinaldi C. Monitoring iron oxide nanoparticle surface temperature in an alternating magnetic field using thermoresponsive fluorescent polymers. *J. Appl. Phys.* 2012; 111: 07B334
88. Eze MO. Phase Transitions in phospholipid bilayers: lateral phase separations play vital roles in biomembranes. *Biochem. Educ.* 1991; 19: 204–208
89. Forbes N, Pallaoro A, Reich NO et al. Rapid, Reversible release from thermosensitive liposomes triggered by near-infra-red light. *Part Part Syst. Charact.* 2014; 31: 1158–1167
90. Paula S, Volkov AG, Van Hoek AN et al. Permeation of protons, potassium ions, and small polar molecules through phospholipid bilayers as a function of membrane thickness. *Biophys J.* 1996; 70: 339–348
91. Huster D, Jin AJ, Arnold K et al. Water permeability of polyunsaturated lipid membranes measured by ^{17}O NMR. *Biophys J.* 1997; 73: 855–864
92. Issa B, Obaidat IM, Hejasee RH, Qadri S, Haik Y. NMR relaxation in systems with magnetic nanoparticles: a temperature study. *J Magn Reson Imaging.* 2014; 39: 648–655.
93. Matteucci M, Anyarambhatla G, Rosner G et al. Hyperthermia increases accumulation of technetium-99m-labeled liposomes in feline sarcomas. *Clin Cancer Res* 2000; 6: 3748–3755
94. Park K, Lee GY, Kim YS et al. Heparin-deoxycholic acid chemical conjugate as an anticancer drug carrier and its antitumor activity. *J. Control. Release* 2006; 114: 300–306
95. Oleson JR, Dewhirst MW, Harrelson JM et al. Tumor temperature distributions predict hyperthermia effect. *Int. J. Radiat. Oncol. Biol. Phys.* 1989; 16: 559–570
96. Cho CH, Sreenivasa G, Plotkin M et al. Tumour perfusion assessment during regional hyperthermia treatment: Comparison of temperature probe measurement with H215O-PET perfusion. *Int. J. Hypertherm.* 2010; 26: 404–411
97. Sun X, Xing L, Clifton Ling C et al. The effect of mild temperature hyperthermia on tumour hypoxia and blood perfusion: Relevance for radiotherapy, vascular targeting and imaging. *Int. J. Hypertherm.* 2010; 26: 224–231